

Least-squares wave-equation inversion of time-lapse seismic data sets – A Valhall case study

Gboyega Ayeni and Biondo Biondi

ABSTRACT

We demonstrate an application of least-squares wave-equation inversion using time-lapse data sets from the Valhall field. We pose time-lapse imaging as a joint least-squares problem that utilizes target-oriented approximations to the Hessian of the objective function. Because this method accounts for illumination mismatches—caused by differences in acquisition geometries—and for band-limited wave-propagation effects, it provides better estimates of production-related changes in reservoir acoustic properties than conventional time-lapse processing methods. We show that our method improves image resolution (compared to migration) and that it attenuates obstruction artifacts in time-lapse images.

INTRODUCTION

Reservoir rock and fluid property changes can be obtained from seismic amplitude and/or travel-time changes. There is a wide range of published work on the most important considerations for time-lapse seismic imaging. For example, Batzle and Wang (1992) and Mavko et al. (2003) outline important rock and fluid relationships; Lumley (1995), Rickett and Lumley (2001), Calvert (2005), and Johnston (2005) discuss important processing and practical applications; and Lefevre et al. (2003), Whitcombe et al. (2004), Zou et al. (2006) and Ebaid et al. (2009) present successful case studies. Because of the recorded successes, time-lapse seismic imaging is now an integral part of many reservoir management projects.

In practice, production-related changes in time-lapse seismic images can be masked by non-repeatability artifacts (e.g., changes in geometry, ambient noise) or by effects of complex overburden (e.g., salt canopy). To correctly interpret time-lapse seismic differences, such artifacts must be attenuated—a prerequisite conventionally achieved through image cross-equalization methods (Rickett and Lumley, 2001). Although cross-equalization methods are well developed and provide reliable results in many practical applications, they are inadequate where large inconsistencies exist between the geometries used to acquire the data sets or where the reservoir overburden is complex. Where these conventional methods fail, wave-equation inversion provides a way to attenuate unwanted artifacts in time-lapse images, thereby enhancing production-related changes.

The proposed method is based on linear least-squares migration/inversion of seismic data sets (Nemeth et al., 1999; Köhl and Sacchi, 2003; Clapp, 2005). Because each iteration of a data-space implementation of least-squares migration/inversion is approximately twice the migration cost, this approach is expensive. However, by posing this problem in the image space, it can be efficiently solved in a target-oriented manner (Valenciano et al., 2006; Tang, 2009). For the time-lapse imaging problem, we can either invert for the complete baseline and monitor images or invert for a static baseline and time-lapse images between surveys. Inputs in the resulting formulations are migrated images (or combinations thereof) and the outputs are the inverted images (or time-lapse images). The operators are a concatenation of target-oriented approximations to the Hessian of the least-squares objective function (Ayeni and Biondi, 2010). We regularize the inversion using spatial (dip) and temporal (difference) constraints. Because we assume that the data contain only primaries, robust multiple/noise attenuation and data preprocessing is required prior to inversion. Furthermore, we assume compaction and velocity changes between surveys are small relative to the baseline; therefore the effects of these—which inherently neglected by migrating all data sets with the baseline velocity—can be removed by multidimensional warping of the monitor images to the baseline.

First, we summarize wave-equation inversion of time-lapse data sets. Then, we apply this method to a subset of the Valhall Life of Field Seismic (LoFS) data with a synthesized obstruction in the monitor. We show that the proposed method improves the image resolution (compared to migration) and that it attenuates obstruction artifacts in time-lapse images.

METHODOLOGY

Given a linearized modeling operator \mathbf{L} , the seismic data \mathbf{d} for survey i due to a reflectivity model \mathbf{m} is

$$\mathbf{d}_i = \mathbf{L}_i \mathbf{m}_i. \quad (1)$$

Assuming we have two data sets (baseline \mathbf{d}_0 and monitor \mathbf{d}_1) acquired at different times over an evolving reservoir, joint least-squares migration/inversion involves solving the following regression:

$$\begin{bmatrix} \mathbf{L}_0 & \mathbf{0} \\ \mathbf{0} & \mathbf{L}_1 \\ \epsilon_0 \mathbf{R}_0 & \mathbf{0} \\ \mathbf{0} & \epsilon_1 \mathbf{R}_1 \\ -\zeta_0 \Lambda_0 & \zeta_1 \Lambda_1 \end{bmatrix} \begin{bmatrix} \mathbf{m}_0 \\ \mathbf{m}_1 \end{bmatrix} \approx \begin{bmatrix} \mathbf{d}_0 \\ \mathbf{d}_1 \\ \mathbf{0} \\ \mathbf{0} \\ \mathbf{0} \end{bmatrix}, \quad (2)$$

where \mathbf{R}_i and Λ_i are the spatial and temporal regularization operators respectively, and ϵ_i and ζ_i are the corresponding regularization parameters. Although we can directly solve equation 2 by minimizing the quadratic-norm of the regression (Ajo-Franklin et al., 2005), we choose to transform it to an image space problem of the

form (Ayeni and Biondi, 2011)

$$\begin{bmatrix} \mathbf{H}_0 & \mathbf{0} \\ \mathbf{0} & \mathbf{H}_1 \\ \hline \mathbf{R}_{00} & \mathbf{0} \\ \mathbf{0} & \mathbf{R}_{11} \\ \hline \Lambda_{00} & -\Lambda_{01} \\ -\Lambda_{10} & \Lambda_{11} \end{bmatrix} \begin{bmatrix} \hat{\mathbf{m}}_0 \\ \hat{\mathbf{m}}_1 \end{bmatrix} \approx \begin{bmatrix} \tilde{\mathbf{m}}_0 \\ \tilde{\mathbf{m}}_1 \\ \hline \mathbf{0} \\ \mathbf{0} \\ \hline \mathbf{0} \\ \mathbf{0} \end{bmatrix}, \quad (3)$$

where $\mathbf{H}_i = \mathbf{L}_i^T \mathbf{L}_i$ is the wave-equation Hessian, and $\mathbf{R}_{ii} = \epsilon_i^2 \mathbf{R}_i^T \mathbf{R}_i$ and $\Lambda_{ij} = \zeta_i \Lambda_i^T \zeta_j \Lambda_j$ are the spatial and temporal constraints. The inverted time-lapse image $\Delta \hat{\mathbf{m}}$ is then the difference between the inverted baseline and monitor images ($\hat{\mathbf{m}}_0$ and $\hat{\mathbf{m}}_1$). Equation 3 can be extended to multiple seismic data sets (Ayeni and Biondi, 2010). Alternatively, we can re-write equation 3 to invert directly for the time-lapse image and a static baseline image (Ayeni and Biondi, 2011). Due to physical movements of reflectors and velocity changes (e.g., due to reservoir depletion and compaction) between surveys, the baseline and monitor images will not be aligned. Such misalignments must be accounted for before or during inversion. As is the case in many practical time-lapse monitoring problems, we assume that the monitor data are migrated with the baseline velocity, which has been estimated to a high accuracy. However this method can be applied where an accurate monitor velocity has been available. The updated inversion problem is then given by (Ayeni and Biondi, 2011)

$$\begin{bmatrix} \mathbf{H}_0 & \mathbf{0} \\ \mathbf{0} & \mathbf{H}_1^b \\ \hline \mathbf{R}_{00} & \mathbf{0} \\ \mathbf{0} & \mathbf{R}_{11}^b \\ \hline \Lambda_{00} & -\Lambda_{01}^b \\ -\Lambda_{10}^b & \Lambda_{11}^b \end{bmatrix} \begin{bmatrix} \hat{\mathbf{m}}_0 \\ \hat{\mathbf{m}}_1^b \end{bmatrix} \approx \begin{bmatrix} \tilde{\mathbf{m}}_0 \\ \tilde{\mathbf{m}}_1^b \\ \hline \mathbf{0} \\ \mathbf{0} \\ \hline \mathbf{0} \\ \mathbf{0} \end{bmatrix}, \quad (4)$$

where $\tilde{\mathbf{m}}_1^b$ and $\hat{\mathbf{m}}_1^b$ are respectively the migrated and inverted monitor images repositioned (warped) to the baseline image. The superscript b on the operators denotes that they are referenced to the baseline image. For example, \mathbf{H}_1^b is the Hessian computed with the monitor geometry but with the baseline velocity. Note that the conventional time-lapse image $\Delta \tilde{\mathbf{m}}^b$ estimated at the baseline position is given by

$$\Delta \tilde{\mathbf{m}}^b = \tilde{\mathbf{m}}_1^b - \tilde{\mathbf{m}}_0, \quad (5)$$

while the inverted time-lapse image $\Delta \hat{\mathbf{m}}^b$ is given by

$$\Delta \hat{\mathbf{m}}^b = \hat{\mathbf{m}}_1^b - \hat{\mathbf{m}}_0. \quad (6)$$

For any practical application, it is infeasible (and unnecessary) to compute the full Hessian matrix. Because the problem is posed in the image space, we only need to compute the Hessian for a target region of interest around the reservoir. In addition, we only compute off-diagonal elements sufficient to capture the dominant structure

of the Hessian. This target-oriented approximation of the Hessian is given by (Valenciano et al., 2006)

$$H(\mathbf{x}_T, \mathbf{x}_{T+\mathbf{a}_x}) = \sum_{\omega} \omega^4 \sum_{\mathbf{x}_s} |f(s)|^2 G(\mathbf{x}_s, \mathbf{x}_T, \omega) \bar{G}(\mathbf{x}_s, \mathbf{x}_{T+\mathbf{a}_x}, \omega) \sum_{\mathbf{x}_r} G(\mathbf{x}_T, \mathbf{x}_r, \omega) \bar{G}(\mathbf{x}_{T+\mathbf{a}_x}, \mathbf{x}_r, \omega), \quad (7)$$

where \mathbf{x}_T is an image point within the target area, and $\mathbf{x}_{T+\mathbf{a}_x}$ represents points within a *small* region around \mathbf{x}_T . For any image point, elements of $\mathbf{H}(\mathbf{x}_T, \mathbf{x}_{T+\mathbf{a}_x})$ represent a row of a sparse Hessian matrix \mathbf{H} whose non-zero components are defined by \mathbf{a}_x . Therefore, \mathbf{a}_x defines the number of off-diagonal elements of the Hessian that are computed — which represents the size of the point spread function (PSF) at each image point (Lecomte and Gelius, 1998; Chavent and Plessix, 1999; Valenciano et al., 2006). \bar{G} is the complex conjugate of Green’s function G at frequency ω ; f_s is the source function; and \mathbf{x}_s and \mathbf{x}_r are the source and receiver positions, respectively. Note that because of symmetry, only one half of the approximate Hessian is required. In this paper, we follow the phase-encoding approach of Tang (2009) to efficiently compute the target-oriented Hessian. The spatial regularization operators in equation 4 are non-stationary directional Laplacians (Hale, 2007), whereas the temporal constraint is the difference between the aligned images. Further review of the methodology is given by Ayeni and Biondi (2010, 2011)

CASE STUDY

We consider a subset of the Life of Field Seismic (LoFS) data sets acquired at Valhall, a giant oil field located in the Norwegian North Sea. There is a wide range of published work on the exploration and development effort in the Valhall field and on different aspects of the LoFS project at Valhall. For example, Munns (1985) discusses Valhall geology in detail; Barkved et al. (2003) discuss the production history and development plans for the field; Barkved (2004) discusses the permanent acquisition array; van Gestel et al. (2008) discuss aspects of the data acquisition, processing, and analysis; and Hatchell et al. (2005) and van Gestel et al. (2011) discuss aspects of the data interpretation and integration with other reservoir data.

In this paper, we consider data from the first (LoFS 1) and the ninth (LoFS 9) surveys acquired in November 2003 and December 2007, respectively. For this study, to avoid imaging challenges caused by a gas cloud located above the crest of the Valhall structure, we choose a subset of the original data covering the Southern flank of the structure. Whereas the original (full) data consists of approximately 50,000 shots and 2400 receivers, the data subset consists of approximately 33,000 shots and 470 receivers. Shots are spaced at 50 m in both the inline and crossline directions, while the receivers, located along 10 permanent cables at approximately 70 m depth, are spaced at 50 m in the inline and 300 m in the crossline directions (Figure 1).

The maximum absolute source-receiver offset is 5 km. The data have been pre-processed, preserving only the up-going primary compressional wave data. To simulate an obstruction, we create a 1.44 sq. km gap in the monitor data at the center of the 9 sq. km study area (Figure 1(b)). Figure 2 shows the resulting common-midpoint (CMP) fold for the complete (baseline) and incomplete (monitor) geometries. Using reciprocity, shot and receiver locations are swapped, such that receiver gathers are treated as shot records. The data are migrated using 320 frequencies (up to 35 Hz) with a split-step one-way wave-equation shot-profile migration algorithm. All data are migrated with the baseline velocity model (Figure 3) obtained—to a satisfactory degree of accuracy—by full waveform inversion (Sirgue et al., 2010). The target area is a small (700 x 3000 x 3000 m) window around the reservoir, located outside the area most affected by the gas cloud. For both the baseline and monitor geometries, we compute the target-oriented Hessian using 64 frequencies spaced equally within the migration frequency band.

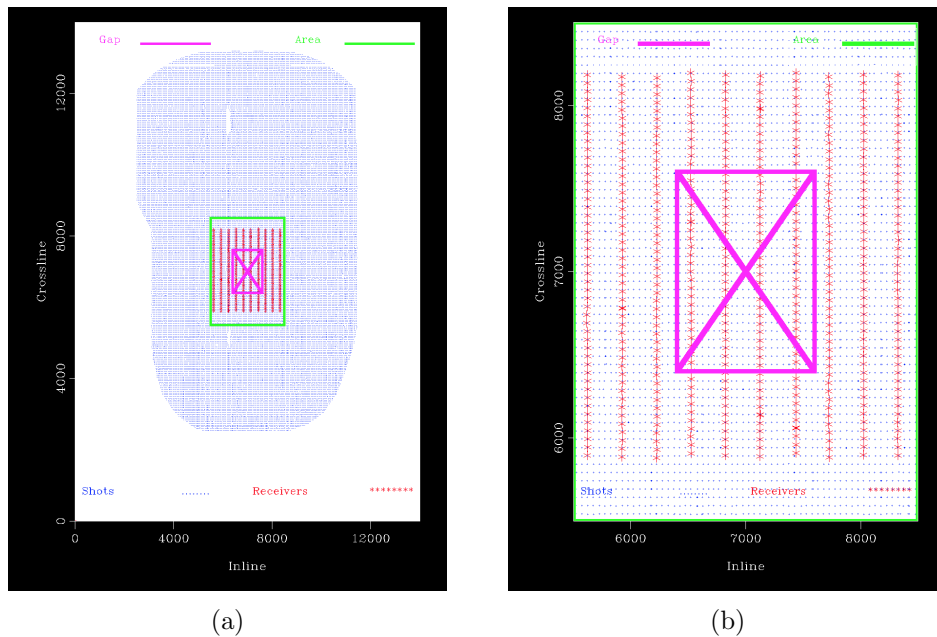


Figure 1: Acquisition geometry showing locations of all shots and receivers (a) and a zoom showing only the study area (b). Apart from the introduction of a gap, the source-receiver geometry is closely repeated for both data sets. Note that the gap is located at the center of the study area. The coordinate axes in these figures (and in all figures) are distances in meters. [CR]

The diagonals of the Hessian matrices (subsurface illumination/fold) for the study area obtained using the complete (baseline) and incomplete (monitor) geometries are shown in Figure 4. Note that in both cases, illumination distribution is highly non-stationary throughout the study area. The ratio between the Hessian diagonals for the two geometries are shown in Figure 5. Note that although the illumination discrepancy is simple at the ocean bottom (Figure 5(a)), this discrepancy becomes

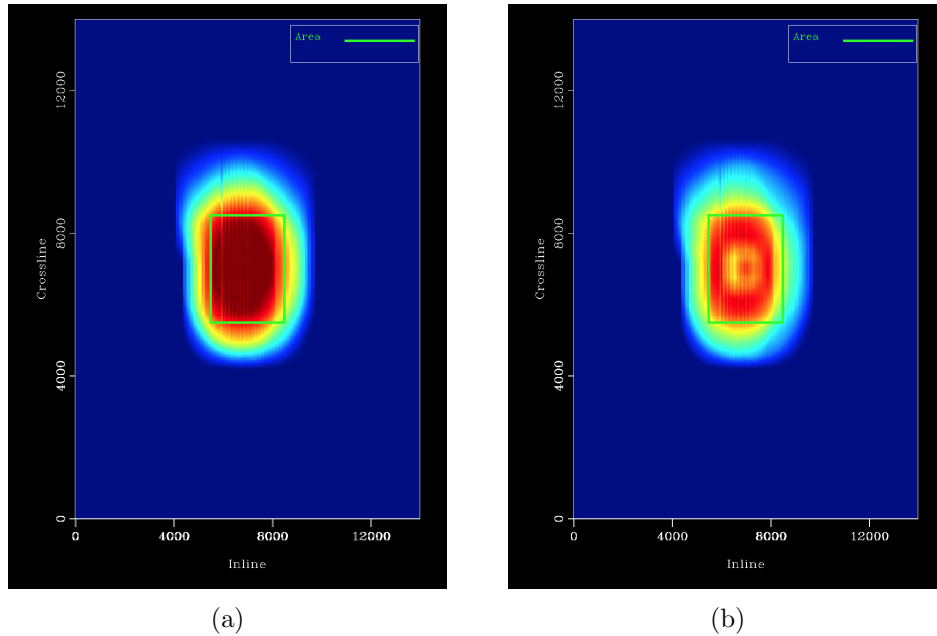


Figure 2: Surface (CMP) fold for the baseline (a) and monitor (b). Red indicates high fold, whereas blue indicates low fold. Note that whereas the baseline fold is mostly uniform within the study area, the gapped monitor geometry causes significant non-uniformity of fold. The box indicates the same study area shown in Figure 1(b). [CR]

highly complex at the reservoir depth (Figure 5(b)).

The migrated baseline and monitor images of the study area are shown in Figure 6. Note that the differences between the images at the reservoir depth are due to a combination of production-related changes and the gap in the monitor data. In addition, the panels in Figure 6 show the target area for inversion. Because of fluid changes caused by production and injection, and compaction caused by pressure depletion, imaging the monitor data with the baseline velocity causes apparent displacements between the baseline and monitor images. Components of the apparent displacements between the baseline and monitor images (Figure 7) are obtained using a cyclic 1D correlation approach (Ayeni, 2011). Before estimating time-lapse images, and prior to inversion, the baseline and monitor are aligned using these apparent displacements. Time-lapse amplitudes extracted within a 60 m window around the reservoir after migration and inversion are shown in Figure 9.

DISCUSSION

A common problem in many time-lapse seismic monitoring studies is the presence of obstructions that create gaps in the monitor data. Such obstructions, usually caused by production and drilling facilities, generate artifacts that contaminate production-

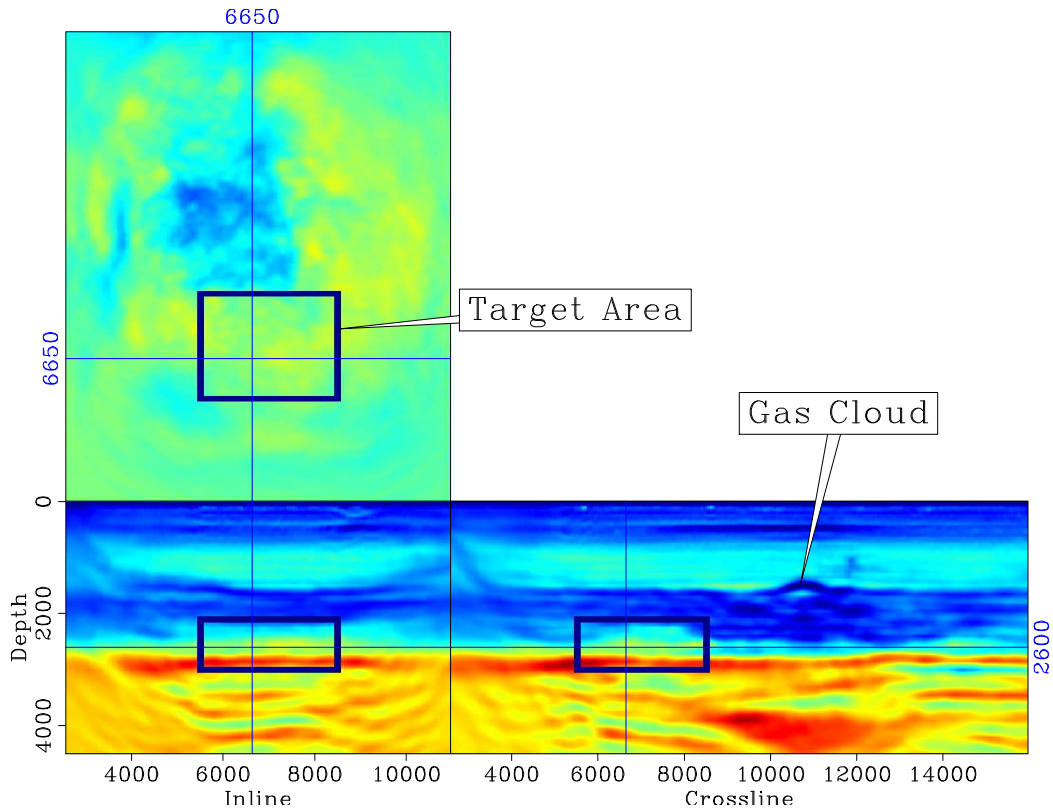


Figure 3: Baseline migration velocity obtained by full waveform inversion (Sirgue et al., 2010). Red indicates high velocity, whereas blue indicates low velocity. This velocity model was used to image all data sets in this study. Note that the target area—indicated by the box—is restricted to a small area of interest around the reservoir. The gas cloud, located outside the study area does not cause significant imaging challenge in the target area. [NR]

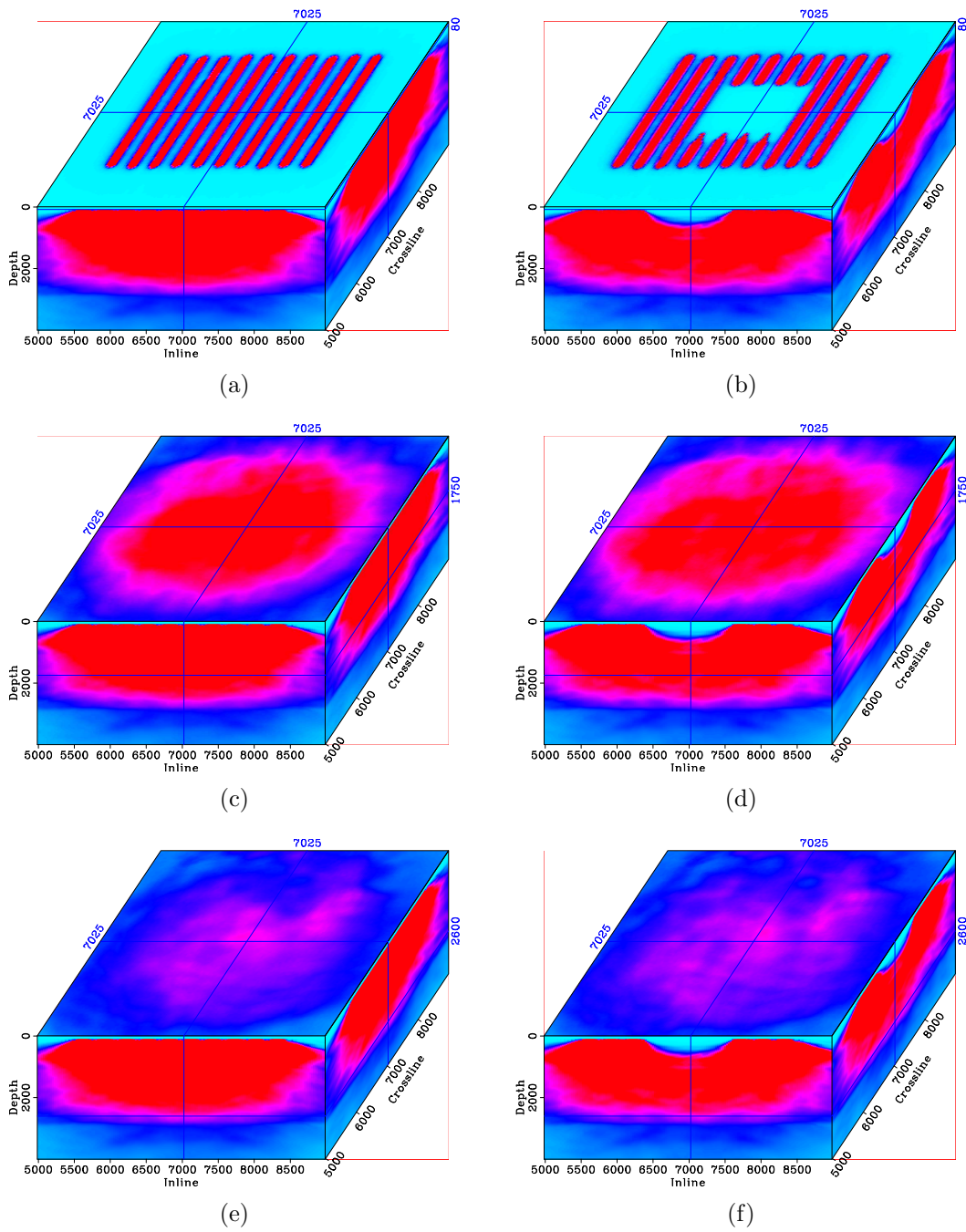


Figure 4: Hessian diagonal for the complete baseline (left) and incomplete monitor (right). In these (and similar) displays throughout this paper, the top panel is a depth slice and the side panels are the inline and crossline slices. The crosshairs show the position of the slices in the image cube. The depth slices show the illumination at the ocean bottom (a) and (b); above the reservoir (c) and (d); and within the reservoir (e) and (f). Note the locations of the complete receiver lines in (a) and the gap in (b). Red indicates high illumination, whereas cyan indicates low illumination. [CR]

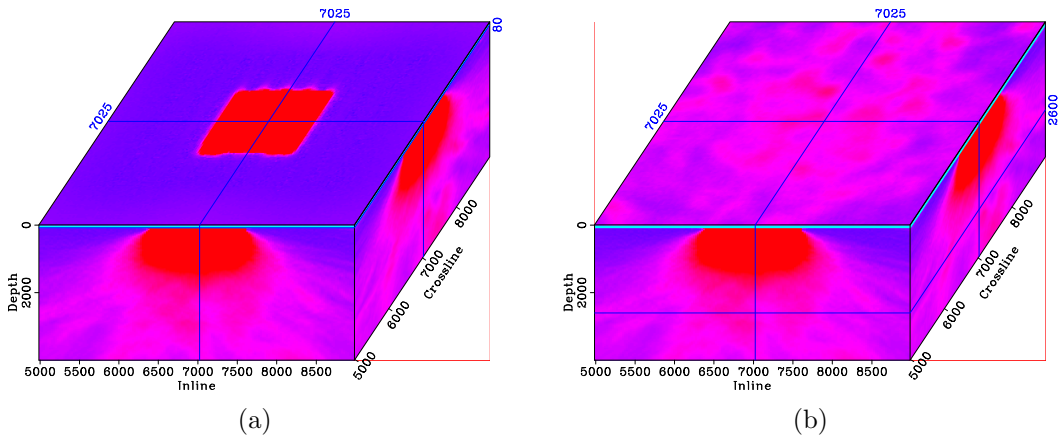


Figure 5: Illumination ratio between the baseline and monitor at the ocean bottom (a) and at the reservoir depth (b). Note that the simple rectangular illumination disparity at the ocean bottom becomes more complex at the reservoir depth. [CR]

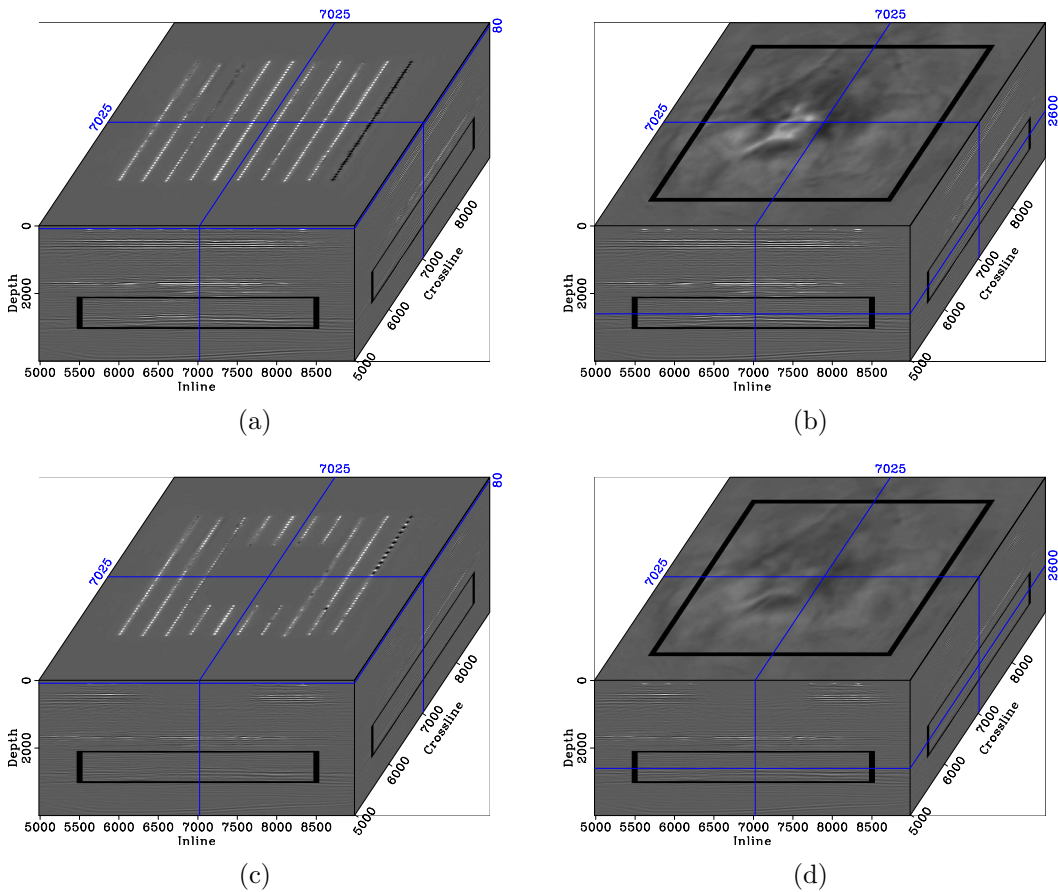


Figure 6: Migrated images showing depth slices at the ocean bottom (left) and at the reservoir depth (right). The box indicates the target area in the baseline image (a) & (b), and in the monitor image (c) & (d). Note the location of the gap in the monitor. [CR]

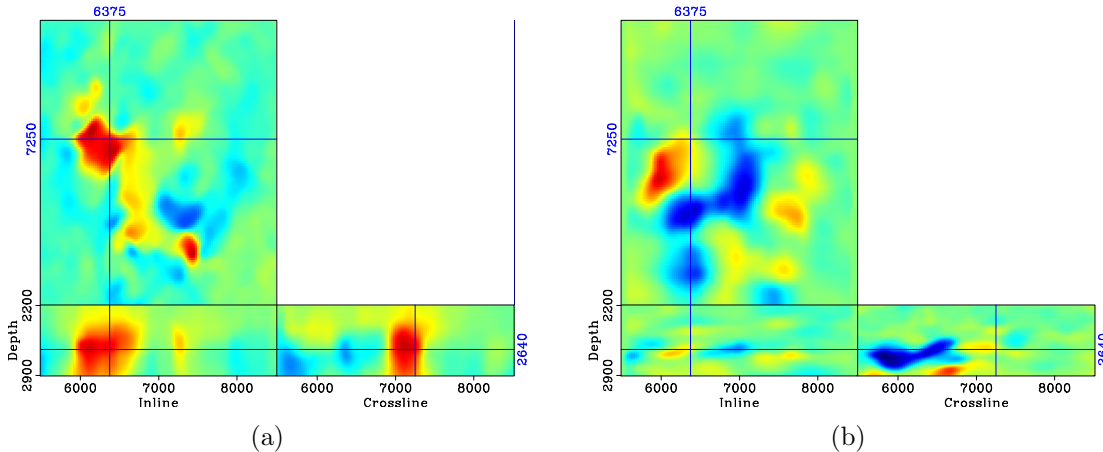


Figure 7: Vertical (a) and inline (b) components of apparent displacement vectors between the baseline and monitor images within the target area. In both Figures, red indicates positive (downward or rightward) apparent displacements, whereas blue indicates negative (upward/leftward) apparent displacements. Similar results were obtained for the crossline displacement components (not shown). Prior to inversion, the baseline and monitor images are aligned using these apparent displacements. [CR]

related seismic amplitudes changes, thereby limiting our ability to accurately interpret observed time-lapse amplitudes. The Valhall LoFS project provides data with high repeatability of both source and receiver locations (Figure 1). Therefore, in this case study, the major source of time-lapse amplitude contamination is the synthesized gap in the monitor data. Because CMP fold provides only limited information about the geometry difference (Figure 2), it is insufficient to compensate for subsurface illumination differences. As shown in Figure 4, the Hessian diagonal provides a robust measure of the subsurface illumination for any given geometry. A measure of the subsurface illumination differences can be obtained from the ratio of the Hessian diagonal for the different survey geometries (Figure 5). Although the Hessian diagonal provides information about subsurface illumination and differences, the band-limited wave-propagation effects are provided by the Hessian off-diagonals (not shown). Because the least-squares problem is in the image space, we are able to solve it for a small target around the reservoir (Figure 6). This enables us to try different combinations of inversion parameters efficiently and to focus on improving the results in the region around the reservoir, where the most important production/injection-related changes are expected. Because the Hessian serves as a geometry- and propagation-dependent deconvolution operator, it provides images with improved resolution compared to migration (Figure 8). Because of the gap in the monitor data, there is a large disparity in the distribution of time-lapse amplitudes in the migrated images (Figures 9(a) and 9(b)). Inversion corrects for this disparity, thereby leading to comparable time-lapse amplitude distributions in both the complete and incomplete data examples (Figures 9(c) and 9(d)).

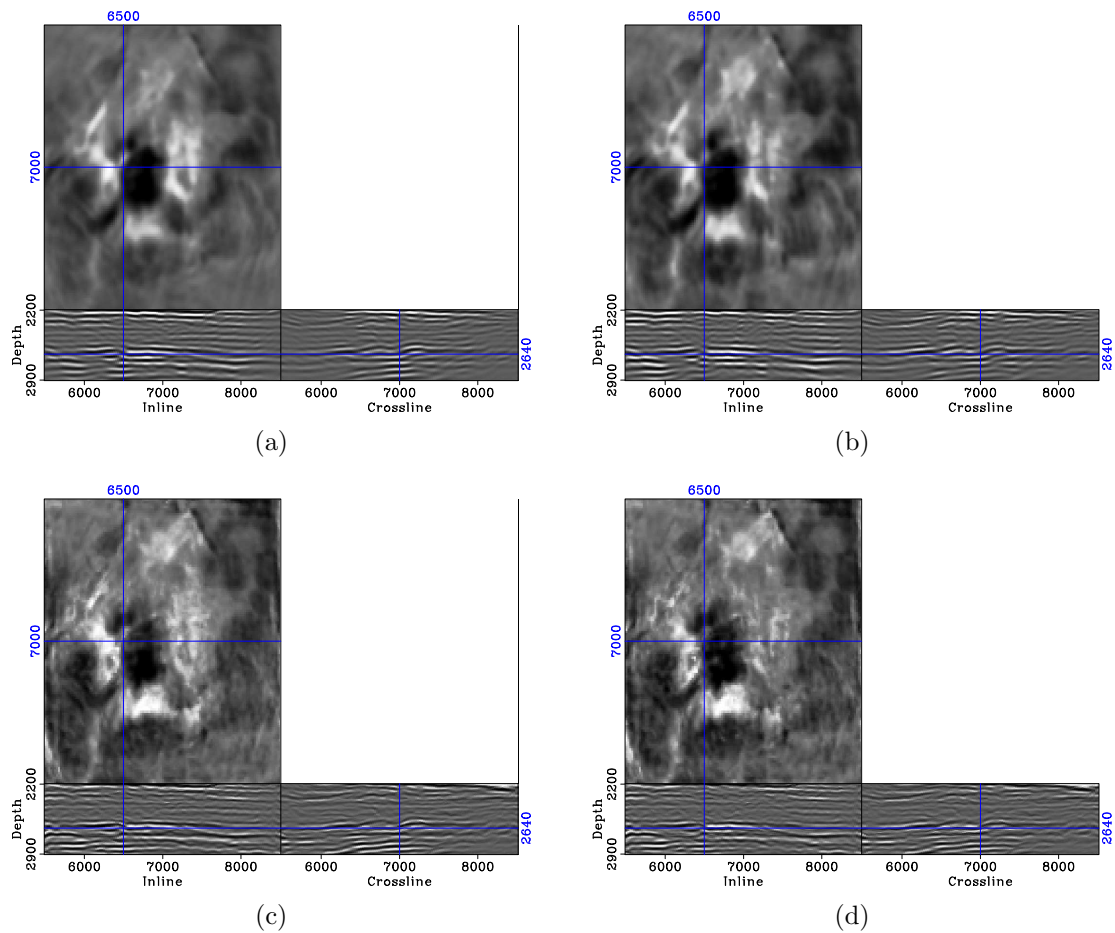


Figure 8: Migrated (a) & (b), and inverted (c) & (d) monitor images for the target area. Panels (a) & (c) are obtained from the complete monitor data, whereas (b) & (d) are obtained from the incomplete (gapped) monitor data. Note that inverted images (c) & (d) show improved resolution over the migrated images (a) & (b). [CR]

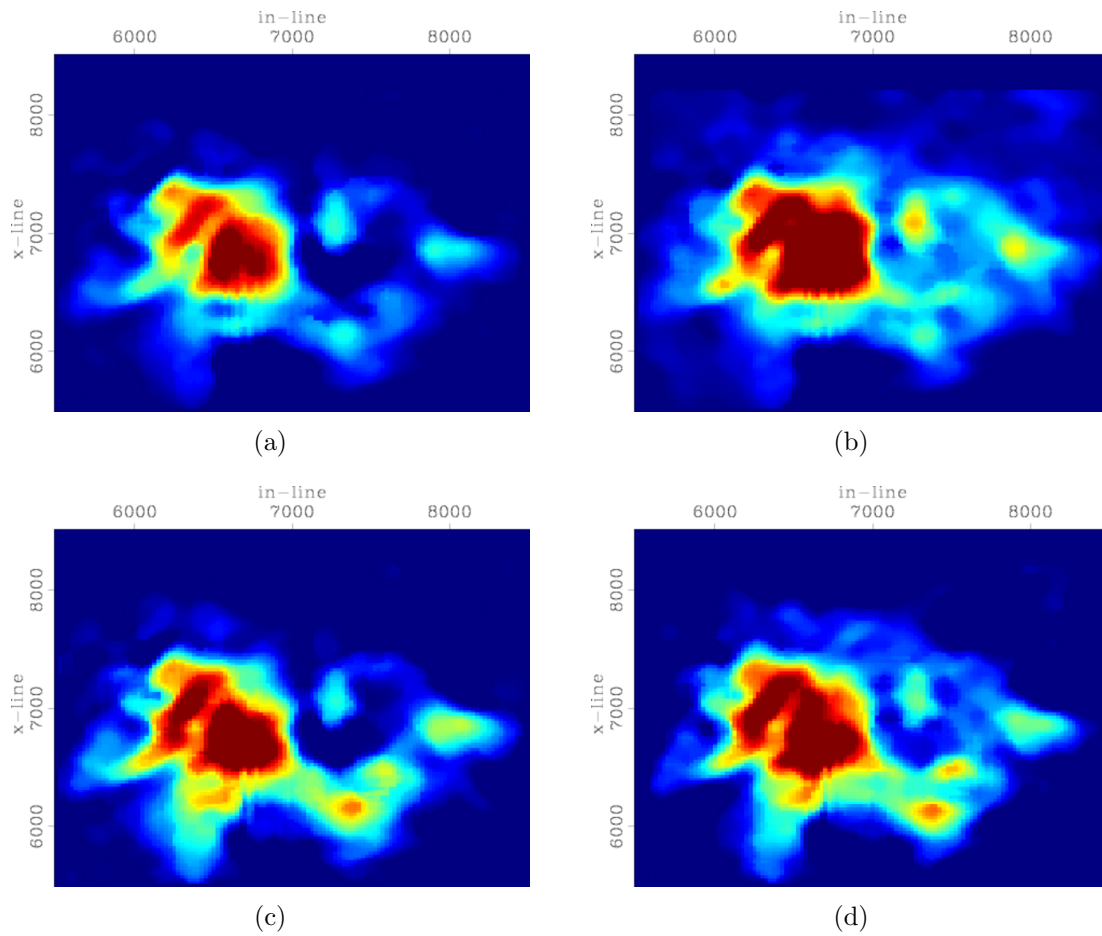


Figure 9: Absolute time-lapse amplitudes in the reservoir obtained from migration (a) & (b), and inversion (c) & (d). Note the discrepancy in the time-lapse amplitude distribution obtained via migration of the complete (a), and incomplete (b) data. Note that this discrepancy has been removed via inversion of the same data sets (c) & (d). [CR]

CONCLUSIONS

Because least-squares wave-equation migration/inversion accounts for illumination mismatches—caused by differences in acquisition geometries—and for band-limited wave-propagation effects, it provides images with improved resolution and better definition of seismic amplitude changes. Using subsets of the Valhall LoFS data, we showed that this method can be used to attenuate artifacts caused by obstructions in the acquisition geometries.

ACKNOWLEDGMENTS

We thank BP and Valhall partners for donating the field data used in this study. We thank the Stanford Center for Computational Earth & Environmental Science (CEES) for providing the computer resources used in this study.

REFERENCES

- Ajo-Franklin, J. B., J. Urban, and J. M. Harris, 2005, Temporal integration of seismic traveltimes tomography: SEG Technical Program Expanded Abstracts, **24**, 2468–2471.
- Ayeni, G., 2011, Cyclic 1D matching of time-lapse seismic data sets: A case study of the norne field: SEG Technical Program Expanded Abstracts, **30**, 4234–4238.
- Ayeni, G. and B. Biondi, 2010, Target-oriented joint least-squares migration/inversion of time-lapse seismic data sets: Geophysics, **75**, R61–R73.
- , 2011, Wave-equation inversion of time-lapse seismic data sets: SEP Report, **143**.
- Barkved, O., P. Heavey, R. Kjelstadli, T. Kleppan, and T. G. Kristiansen, 2003, Valhall Field - still on plateau after 20 years of production: Offshore Europe, **1**.
- Barkved, O. I., 2004, Continuous seismic monitoring: SEG Technical Program Expanded Abstracts, **23**, 2537–2540.
- Batzle, M. and Z. Wang, 1992, Seismic properties of pore fluids: Geophysics, **57**, 1396–1408.
- Calvert, R., 2005, Insights and methods for 4D reservoir monitoring and characterization: SEG/EAGE DISC (Distinguished Instructor Lecture Course).
- Chavent, G. and R. E. Plessix, 1999, An optimal true-amplitude least-squares prestack depth-migration operator: Geophysics, **64**, 508–515.
- Clapp, M. L., 2005, Imaging under salt: illumination compensation by regularized inversion: PhD thesis, Stanford University.
- Ebaid, H., M. Nasser, P. Hatchell, and D. Stanley, 2009, Time-lapse seismic makes a significant business impact at Holstein: SEG, Expanded Abstracts, **28**, 3810–3814.
- Hale, D., 2007, A method for estimating apparent displacement vectors from time-lapse seismic images: CWP Report-566.
- Hatchell, P., R. Kwar, and A. Savitski, 2005, Integrating 4d seismic, geomechan-

- ics and reservoir simulation in the Valhall oil field: 67th EAGE Conference and Exhibition Extended abstract,.
- Johnston, D., 2005, Time-lapse 4D technology: Reservoir surveillance: AAPG Search and Discovery.
- Kühl, H. and M. D. Sacchi, 2003, Least-squares wave-equation migration for avp/ava inversion: *Geophysics*, **68**, 262–273.
- Lecomte, I. and L.-J. Gelius, 1998, Have a look at the resolution of prestack depth migration for any model, survey and wavefields: SEG Technical Program Expanded Abstracts, **17**, 1112–1115.
- Lefeuvre, F., Y. Kerdraon, J. Peliganga, S. Medina, P. Charrier, R. L’Houtellier, and D. Dubucq, 2003, Improved reservoir understanding through rapid and effective 4D: Girassol field, Angola, West Africa: SEG Technical Program Expanded Abstracts, **22**, 1334–1337.
- Lumley, D. E., 1995, Seismic time-lapse monitoring of subsurface fluid flow: PhD thesis, Stanford University, <http://sepwww.stanford.edu/public/docs/sep91/>.
- Mavko, G., T. Mukerji, and J. Dvorkin, 2003, *The rock physics handbook: Tools for seismic analysis of porous media*: Cambridge University Press.
- Munns, J., 1985, The Valhall field: a geological overview: *Marine and Petroleum Geology*, **2**, 23 – 43.
- Nemeth, T., C. Wu, and G. T. Schuster, 1999, Least-squares migration of incomplete reflection data: *Geophysics*, **64**, 208–221.
- Rickett, J. E. and D. E. Lumley, 2001, Cross-equalization data processing for time-lapse seismic reservoir monitoring: A case study from the Gulf of Mexico: *Geophysics*, **66**, 1015–1025.
- Sirgue, L., O. Barkved, J. Dellinger, J. Etgen, U. Albertin, and J. Kommedal, 2010, Full waveform inversion: the next leap forward in imaging at Valhall: *First Break*, **28**.
- Tang, Y., 2009, Target-oriented wave-equation least-squares migration/inversion with phase-encoded hessian: *Geophysics*, **74**, WCA95–WCA107.
- Valenciano, A. A., B. Biondi, and A. Guitton, 2006, Target-oriented wave-equation inversion: *Geophysics*, **71**, A35–A38.
- van Gestel, J.-P., K. D. Best, O. I. Barkved, and J. H. Kommedal, 2011, Integration of the life of field seismic data with the reservoir model at the Valhall field: *Geophysical Prospecting*, **59**, 673–681.
- van Gestel, J.-P., J. H. Kommedal, O. I. Barkved, I. Mundal, R. Bakke, and K. D. Best, 2008, Continuous seismic surveillance of Valhall field: *The Leading Edge*, **27**, 1616–1621.
- Whitcombe, D. N., J. M. Marsh, P. J. Clifford, M. Dyce, C. J. S. McKenzie, S. Campbell, A. J. Hill, R. S. Parr, C. Pearse, T. A. Ricketts, C. P. Slater, and O. L. Barkved, 2004, The systematic application of 4D in BP’s North-West Europe operations — 5 years on: SEG Technical Program Expanded Abstracts, **23**, 2251–2254.
- Zou, Y., L. R. Bentley, L. R. Lines, and D. Coombe, 2006, Integration of seismic methods with reservoir simulation, Pikes Peak heavy-oil field, Saskatchewan: *The Leading Edge*, **25**, 764–781.

